

The effect of Sr and Mg substitutions on the mechanical properties and solubility of the fluorapatite ceramics for biomedical applications

M. Hossein Ghaemi (✉ ghaemi@pg.edu.pl)

Gdańsk University of Technology: Politechnika Gdanska <https://orcid.org/0000-0003-2735-4848>

Sergiy Y. Sayenko

NSC Kharkov Institute Physics & Technology NASU

Volodymyr Shkuropatenko

NSC Kharkov Inst. Physics & Tech. NASU

Anna Zykova

NSCAD: NSCAD University Physics and Technology NASU

Kateryna Ulybkina

Adichunchanagiri Institute of Technology Department of Physics

Olena Bereznyak

NSC Kharkov Institute Physics and Technology NASU

Andrzej Krupa

Institute of Fluid Flow Machinery, Polish Academy of Science

Mirosław Sawczak

Institute of Fluid Flow Machinery, Polish Academy of Science

Research Article

Keywords: Ceramics, fluorapatites, mechanical properties, solubility, biocompatibility

Posted Date: December 10th, 2020

DOI: <https://doi.org/10.21203/rs.3.rs-123802/v1>

License:   This work is licensed under a Creative Commons Attribution 4.0 International License.

[Read Full License](#)

Abstract

The ionic substitutions play important role in the modifications of the biological apatites. Recently, the attention has been focused on the co-doping effects of additives on the functional properties of apatite based biomaterials. Under a research work for which the results are presented here, the dense samples of fluorapatites: $\text{Ca}_{10}(\text{PO}_4)_6\text{F}_2$ and $\text{Ca}_8\text{MgSr}(\text{PO}_4)_6\text{F}_2$ were produced after sintering at a temperature of 1250 °C for 6 hours in air. The XRD, IR and Raman spectrometry results show a high crystallinity of the fluorapatite and strontium-magnesium-doped fluorapatites. The results demonstrate the stability of structural and mechanical properties of fluorapatites after immersion tests in saline and buffer solutions. The durability of mechanical properties and biocompatibility of $\text{Ca}_{10}(\text{PO}_4)_6\text{F}_2$ and $\text{Ca}_8\text{MgSr}(\text{PO}_4)_6\text{F}_2$ fluorapatites make these materials highly attractive for biomedical application.

Highlights

Mono phase nanopowders of $\text{Ca}_{10}(\text{PO}_4)_6\text{F}_2$ and $\text{Ca}_8\text{MgSr}(\text{PO}_4)_6\text{F}_2$ fluorapatites were produced by chemical precipitation method

Sintering of $\text{Ca}_8\text{MgSr}(\text{PO}_4)_6\text{F}_2$ fluorapatite at 1250 °C resulted in increase of formation of $\text{Ca}_3(\text{PO}_4)_2$ concomitant phase

Dissolution of the fluorapatites occurs due to Ca and F surface depletion

Structural and mechanical stability in saline solutions allow to present fluorapatites as a perspective material for biomedical applications.

1. Introduction

Minerals and synthetic compounds with a structural type of apatite are widely used in many fields, including construction and electronic industries. Such materials also serve as catalysts and ion exchangers in the chemical industry. Apatites activated by rare earth elements are used as luminescent and laser materials. Moreover, apatite materials are considered as promising materials for immobilization of high-level waste (HLW) due to high chemical and radiation resistance and a wide range of structural iso- and heterovalent substitutions [1,2].

Some types of apatite materials have found wide application in orthopedics and dentistry due to the composition close to inorganic components of human bones and teeth [3-5].

Biological apatites, including hydroxyapatite ($\text{Ca}_{10}(\text{PO}_4)_6(\text{OH})_2$, HAp) have been widely used in the biomedical fields due to their bioactivity, biocompatibility and osteoconductive properties [6]. Recently, a large number of attempts have been made to the modification of biological apatites properties, such as biocompatibility, mechanical properties and solubility. Natural apatites contain various amounts of substitutions (F^- , CO_3^{-2} , Sr^{+2} , Mg^{+2} , Zn^{+2}) [7-9]. Fluorine-substituted HAp ($\text{Ca}_{10}(\text{PO}_4)_6(\text{OH})_x\text{F}_{2-x}$, FHAp)

and fluorapatite ($\text{Ca}_{10}(\text{PO}_4)_6\text{F}_2$, FAp) have low solubility and good biocompatibility [10,11]. The incorporation of fluorine into apatite lattice makes the apatite structure more stabilized, a quite well-ordered apatite structure was formed [12]. Fluorine replacement can favor the crystallization of calcium phosphate, improve the chemical stability and decrease the mineral dissolution [13,14]. In addition, substitution of OH^- groups by F^- results in a better protein adsorption and cell attachment [15]. Fluoride in saliva and blood plasma is necessary for dental and skeletal development and plays a very important role in stimulating the processes of proliferation and differentiation of bone cells. The osteoblast responses were improved through fluoride incorporation [16].

Despite the fact, that apatites are widely proposed as biocompatible and osteoconductive materials, but they demonstrate some principal limitations for long-term clinical applications. A large number of studies have been made to enhance their mechanical properties, such as brittleness and mechanical strength. It is shown that the ionic substitutions in biological apatites play a key role in enhancing such functional properties as biocompatibility and mechanical strength [17-19].

Strontium (Sr), a trace element chemically close to calcium, is mainly incorporated into bone by two mechanisms: surface exchange or ionic substitution. Bone mineral consists of a poorly crystalline fraction made of apatite and calcium phosphate complexes. The strontium levels in bone are varied according to the bone structure. Furthermore, at the crystal level, higher Sr concentrations are observed in newly formed bone than in old bone [20].

There is experimental evidence that strontium induces pharmacological actions on bone metabolism [21,22]. The strontium ability to substitute calcium in the hydroxyapatite crystal lattice has been previously demonstrated [23]. Strontium has also been incorporated in the structure of new bioactive materials, and is used as a drug in the form of strontium ranelate to increase the densification of bone in osteoporotic patients. In vivo studies of Sr bioactive glasses [24] have shown that strontium has a dual function within bone remodeling. It is able to uncouple the process of bone resorption and bone formation by inhibiting osteoclasts and stimulating osteoblasts, respectively. Sr substituted calcium phosphate cements/ceramics were used in orthopedic, in filling bone defects [25]. The composite materials by adding 1 wt.% SrO to biogenic hydroxyapatite (HAp) or hydroxyapatite of biogenic origin - BHAp) have been proposed by Kuda et al [26]. It was found that BHAp/glass/SrO composite possessed a higher porosity and rate of dissolution in a physiologic solution. A beneficial effect of low doses of stable strontium in the treatment of osteoporosis age-related bone diseases was reported. The strontium-induced increase of bone formation results in a better mechanical resistance of bones. The Sr-doped ceramics materials were considered for the development of coating or composite biomaterials to expand the range of biomedical applications [26].

In turn, magnesium (Mg) is one of the most important cationic substitutions for calcium in biological apatites. Dentin, enamel and bone contain 1.23, 0.44 and 0.72 wt.% of Mg, respectively. Over 100 enzymes require the presence of magnesium ions for their catalytic actions. These facts make Mg one of the essential elements for all living organisms [27]. Magnesium is closely relevant to mineralization of

calcified tissue and indirectly influences mineral metabolism [28]. Magnesium deficiency affects all skeletal metabolism stages such as bone growth and bone fragility [29]. Fluorine-substituted HAp, FAp, and Mg-substituted apatites have received increasing attentions in the field of biomedicine. Mg²⁺ substituted FAp provides greater biocompatibility and better biological properties than pure FAp or HAp. The formation and attachment of biomimetic Ca-P coatings in the Simulated Body Fluid (SBF) solution were strongly related to Mg²⁺ content, where Mg-substitution improves the bioactivity of apatite in SBF [13]. In addition, Mg ion promotes bone-like apatite nucleation and growth on titanium surface in SBF solution and improves MC3T3-E1 (E1 type of MC3T3 is an osteoblast precursor [cell line](#) derived from [Mus musculus](#) of mouses [calvaria](#)) cell proliferation [30].

From the other side, recently, the attention has been focused on the co-doping effects of additives on the chemical dissolution behavior of biomaterials. Melt-derived Sr-containing polyphosphate glasses, doped with Mg and Ti were investigated by D. Weiss et al [31]. The inclusion of Mg and Ti was found to increase the bonding strength between phosphate chains resulting in a higher stiffness, better mechanical properties, and lower degradation rates in buffer solution. The properties of different melt-derived alkali-free phosphosilicate glass compositions co-doped with Zn²⁺ and Sr²⁺ ions were investigated in [32]. The compounds showed lower solubility as a result of the ionic field strength associated with its constituent ions. There was a significant difference in the leaching of Zn²⁺ and Sr²⁺ ions in SBF and buffer solution, with a higher rate of release for Sr. Additionally, the substitution of SrO with CaO led to the partial replacement of Ca²⁺ by Sr²⁺ in the fluorapatite and diopside crystal structures [33].

The effect of Sr and Mg substitutions in melt-derived glasses system of CaO-P₂O₅-Na₂O was investigated by M. Stefanic et al [34]. The chemical durability of glasses in water was found to decrease with decreasing Sr content, and it was characterized by linear degradation and highly controllable profiles. The incorporation of Sr and Mg ions improve the solubility, bioactivity and mechanical properties of the glass-ceramics composite system. It was demonstrated that most Mg ions remained in the glass matrix and had a negative effect on the crystallization of apatite with a high Ca/P ratio. On the other side, the presence of Sr element was detected in all the deposited apatites, indicating that the introduced strontium was capable to substitute into the forming apatite nuclei and favor the formation of apatite crystallization.

In addition to biocompatible properties of calcium phosphate ceramics, the antibacterial effect of Sr and Mg substitution has not been well-understood and is an open issue of research. An inhibitory effect of Sr additives on various strains such as Escherichia Coli (E. coli) and Porphyromonas gingivalis (P. gingivalis) was reported in [35]. D. S. Brauer et al [36] shew that the bactericidal action of bone cements was increased via Sr substitution. The samples containing small amounts of Sr (2.5 mol%) reduced the number of bacteria (Streptococcus faecalis) up to one order of magnitude as compared to Sr-free samples. On the other hand, fluorine ions are known to affect the mineralization and bone formation in vivo, resulting from their antibacterial effect. It can be concluded that Sr²⁺ and Mg²⁺ ions have a synergistic effect with F⁻ ions in promoting the antibacterial activity.

Mg and Sr substituted phosphate ceramics and glasses are very attractive materials for the production of modern implants, prosthesis for orthopedic, dental surgery and scaffolds for tissue engineering applications [37]. It is well-known that the dissolution of ceramics in biological environment is complex and depends on numerous factors, such as phase composition, density, and surface parameters. Thus, a further focus on the effect of Sr and Mg co-doped ions on the structural and mechanical properties of calcium phosphate ceramics is of great interest. The aim of the present study was the evaluation of the effect of Sr and Mg ions substitutions on the mechanical properties and solubility of the fluorapatite ceramic.

2. Materials And Methods

Fluorapatite $\text{Ca}_{10}(\text{PO}_4)_6\text{F}_2$ and strontium-magnesium-doped fluorapatite $\text{Ca}_8\text{MgSr}(\text{PO}_4)_6\text{F}_2$ were prepared by chemical precipitation as previously presented in [2]. The following chemically pure reagents were used: $\text{Ca}(\text{NO}_3)_2 \cdot 4\text{H}_2\text{O}$ calcium nitrate, $(\text{NH}_4)_2\text{HPO}_4$ disubstituted ammonium phosphate, NH_4F ammonium fluoride, $\text{Sr}(\text{NO}_3)_2$ strontium and $\text{Mg}(\text{NO}_3)_2$ magnesium nitrates for strontium-magnesium-doped fluorapatite. The final fluorapatite samples were prepared and tested as follows:

- a. **Sintering** of fluorapatite samples was carried out in air in a Nabertherm GmbH L5/13/B180 furnace. In order to produce fluorapatite structures with higher density, the samples were sintered in the temperature range 1000–1250 °C for 6 hours in air.
- b. Samples were **formed** by the method of cold double-sided axial pressing in a hydraulic press.
- c. Differential-thermal analysis and thermogravimetric analysis (**DTA/TGA**) were performed on a SDT Q600 V20.9 Build 20 Thermal analyzer.
- d. The **phase compositions** were studied by X-ray phase analysis (XRD) on a DRON-4-07 in copper radiation.
- e. The **apparent density** (r_{ap}) of the samples after sintering was determined by hydrostatic weighing method.
- f. Transparent electron microscopy (**TEM**) images of the fluorapatite powders were made by transmission microscope TEM 123K.
- g. The **microstructure and chemical composition** of obtained ceramic materials were analysed by Scanning Electron Microscopy (SEM) and Energy Dispersive X-ray (EDX) spectroscopy (Zeiss Evo-40).
- h. **IR spectrometer** IRS-29 (LOMO) was used to record absorption spectra in the IR range. Spectra were detected in the spectral range 4000–400 cm^{-1} (mid-infrared region).
- i. **Raman spectra** were analyzed by a Raman spectroscopy method on confocal microscope (Renishaw inVia).
- j. **Mechanical properties tests** of fluorapatite samples for evaluation of Vickers hardness parameters and elastic modulus were performed by nanoindentation method on a NanoIndenter G200. The

average values were evaluated as result of 10 prints at a depth of 1 μm on the surface of samples. Fracture toughness K_{1c} using Vickers indenter has been studied, as well.

- k. The **dissolution tests** of fluorapatite samples were carried out by immersion in saline or sodium phosphate buffer solution (NaCl - 8, KCl - 0.2, Na_2HPO_4 - 1.44, KH_2PO_4 - 0.24 g/l, pH = 7.4) at a temperature of 37 $^\circ\text{C}$. After 1, 3, 7, and 14 days of testing, the samples were weighed and weight losses divided by the total surface of the sample (Dw/S , mg/dm^2) were determined.
- l. The **fractured surfaces** were observed by SEM and laser confocal microscope methods (Olympus Lext OLS4100) after immersion tests.

3. Results And Analysis

The XRD results of powder of strontium-magnesium-doped fluorapatite $\text{Ca}_8\text{MgSr}(\text{PO}_4)_6\text{F}_2$ obtained by co-precipitation of solutions of the starting components are shown in Fig. 1. An analysis of the diffraction patterns of the obtained powders indicates that, as a result of chemical precipitation, single-phases of fluorapatites $\text{Ca}_8\text{MgSr}(\text{PO}_4)_6\text{F}_2$ were produced in a good agreement with previous results for $\text{Ca}_{10}(\text{PO}_4)_6\text{F}_2$ powders [2]. XRD patterns line demonstrate a significant broadening for $\text{Ca}_8\text{MgSr}(\text{PO}_4)_6\text{F}_2$ powder. This fact is an evidence of small sizes of coherent scattering regions (CSR). The substructure characteristics analysis has shown that the size of CRS for the fluorapatites was in the range of 30-33 nm.

These results are in good agreement with the data of the previous study [38]. As can be seen in transparent electron microscopy (TEM) images (Fig.2), powders of $\text{Ca}_{10}(\text{PO}_4)_6\text{F}_2$ fluorapatite synthesized by chemical precipitation method were agglomerated and mainly consisted from the nano crystalline particles with the average size of 20-30 nm (Fig. 2a). The $\text{Ca}_8\text{MgSr}(\text{PO}_4)_6\text{F}_2$ fluorapatite powders produced by chemical precipitation method were also agglomerated with larger particles of the average size of 50-60 nm. (Fig. 2b).

As it is shown [39], ionic radius of the Sr^{2+} (1.13 \AA) is slightly bigger than of the Ca^{2+} (0.99 \AA) one. On the contrary, ionic radius of the Mg^{2+} (0.65 \AA) is significantly smaller than of Ca^{2+} , and ionic substitution of the calcium by magnesium ions leads to noticeable decrease in lattice parameters of fluorapatite. At present study, the substitutions of the Ca^{2+} by the Sr^{2+} and Mg^{2+} ions in the synthesized $\text{Ca}_{10}(\text{PO}_4)_6\text{F}_2$ powders led to the increasing of fluorapatite lattice parameters: $a = 9.393\text{\AA}$; $c = 6.894\text{\AA}$.

The differential thermal and thermogravimetric analysis (DTA/TGA) curves of powders $\text{Ca}_{10}(\text{PO}_4)_6\text{F}_2$ and $\text{Ca}_8\text{MgSr}(\text{PO}_4)_6\text{F}_2$ produced by chemical co-precipitation have a similar character (Fig. 3). The obtained data indicate the presence of two thermal effects. The first one relates to the removal of adsorbed water at a temperature of ~ 60 -110 $^\circ\text{C}$. The second may be associated with the thermal decomposition of fluorapatites by the reaction [40]:



For fluorapatite, the partial decomposition temperature was near 900 °C (Fig 3a). The partial decomposition temperature of fluorapatite $\text{Ca}_8\text{MgSr}(\text{PO}_4)_6\text{F}_2$, however, decreases to 650 °C, when calcium is replaced by strontium and magnesium (Fig 3b).

The phase composition of sintered (1250 °C, 6 hours) strontium-magnesium-doped fluorapatite sample was represented by the main phase $\text{Ca}_8\text{MgSr}(\text{PO}_4)_6\text{F}_2$ (Fig. 4). The weight content of the $\text{Ca}_8\text{MgSr}(\text{PO}_4)_6\text{F}_2$ phase was about 81.6 wt%. The presence of tricalcium phosphate $\text{Ca}_3(\text{PO}_4)_2$ concomitant phase for strontium-magnesium-doped fluorapatite sample as a result of the process of Ca substitution by Mg and Sr ions was detected.

According to the density measurements (r_{ap}), it is found that the maximum relative densities of fluorapatites $\text{Ca}_{10}(\text{PO}_4)_6\text{F}_2$ and $\text{Ca}_8\text{MgSr}(\text{PO}_4)_6\text{F}_2$ were recorded after sintering at a temperature of 1250 °C are 92% and 94% (2.95 and 3.14 g/cm³), respectively. A slight increase in the density of the $\text{Ca}_8\text{MgSr}(\text{PO}_4)_6\text{F}_2$ sample compared to $\text{Ca}_{10}(\text{PO}_4)_6\text{F}_2$ is possibly due to the presence of a some amount of calcium fluoride CaF_2 [40] and tricalcium phosphate $\text{Ca}_3(\text{PO}_4)_2$. As known from the phase diagram of the calcium fluoride and the tricalcium phosphate, an eutectic between CaF_2 and $\text{Ca}_{10}(\text{PO}_4)_6\text{F}_2$ phases is formed near the temperature of 1200 °C. This effect results in liquid phase formation and more intensification of the sintering process for the $\text{Ca}_8\text{MgSr}(\text{PO}_4)_6\text{F}_2$ fluorapatite. The observed increase of density of strontium-magnesium-doped fluorapatite in comparison to fluorapatite samples may be related to liquid phase sintering of the $\text{Ca}_8\text{MgSr}(\text{PO}_4)_6\text{F}_2$ fluorapatite.

SEM images of cleaved fluorapatite samples confirm the homogeneous structure of fluorapatite and strontium-magnesium-doped fluorapatite, see Fig. 5. As can be seen, a large number of small pores are presented on the cleaved surface of $\text{Ca}_{10}(\text{PO}_4)_6\text{F}_2$, while a smaller number of pores, but with larger dimensions, are observed on the cleaved surface of $\text{Ca}_8\text{MgSr}(\text{PO}_4)_6\text{F}_2$. This difference is attributed to the realization of the liquid-phase sintering mechanism during heat treatment of the $\text{Ca}_8\text{MgSr}(\text{PO}_4)_6\text{F}_2$ sample at the temperature of 1250 °C for 6 hours.

The EDX analysis data of the selected sites of cleaved surface of the $\text{Ca}_{10}(\text{PO}_4)_6\text{F}_2$ and $\text{Ca}_8\text{MgSr}(\text{PO}_4)_6\text{F}_2$ samples are presented in Fig 6. The peaks of Ca, P, O, F, Sr and Mg correspond to the peaks of the main fluorapatites elements. The EDX analysis data have shown some deviations from the calculated values of the consisting elements of both fluorapatite (Ca = 34.15; Sr = 8.29; P = 17.61; O = 36.35; F = 3.60 wt.%) and strontium-magnesium fluorapatite (Ca = 30.82; Sr = 8.42; Mg = 2.33; P = 17.88; O = 36.9; F = 3.65 wt.%).

Fig. 7 shows the data of IR spectroscopy of fluorapatite samples $\text{Ca}_{10}(\text{PO}_4)_6\text{F}_2$ and $\text{Ca}_8\text{SrMg}(\text{PO}_4)_6\text{F}_2$ after sintering. The fluorapatite spectrum contains a series of intense bands with narrow, clear maximum which are typical behavior for the fluorapatite. The spectrum demonstrates the bands of 3450 and 475 cm⁻¹, associated with the presence of adsorbed H₂O given in Table 1. In contrast to fluorapatite, a number of differences were observed in the spectrum of strontium-magnesium-doped fluorapatite:

- a characteristic peak of 725 cm^{-1} appears, corresponding to symmetric vibrations of the bridging bonds of the P-O-P diorthogroups. This indicates the association of phosphate tetrahedra;
- the band disappears in the region of 960 cm^{-1} . This is caused by the degeneracy of the stretching vibrations of the PO_4^{3-} ion due to a change in the coordination environment and symmetry of the PO_4^{3-} ion due to the breaking of bonds between the phosphate tetrahedron and calcium ions;
- significant reduction in the intensity of all bands for the spectrum associated with both the structure of fluorapatite and adsorbed water.

There was detected, that the Sr and Mg doping of fluorapatite results in reduction of the band intensity and band resolution corresponding to PO_4^{3-} vibration modes. This fact has suggested that Ca is substituted by Sr and Mg in the fluorapatite lattice.

Table 1. Assignment of the bands in the IR spectra of fluorapatite samples

$\text{Ca}_{10}(\text{PO}_4)_6\text{F}_2$	$\text{Ca}_8\text{SrMg}(\text{PO}_4)_6\text{F}_2$	Bands [41]
475 cm^{-1}	$460\text{ cm}^{-1}, 480\text{ cm}^{-1}$	Vibrations of OH^- groups replacing F^- in apatite structure
575 cm^{-1}	575 cm^{-1}	Bending vibrations of PO_4^{3-} tetrahedra
610 cm^{-1}	605 cm^{-1}	
	725 cm^{-1}	Symmetric vibrations of bridging bonds P-O diorthogroups
965 cm^{-1}		Stretching vibrations of PO_4^{3-} tetrahedra
1040 cm^{-1}	1040 cm^{-1}	
1090 cm^{-1}	1100 cm^{-1}	
3450 cm^{-1} (~10%)	3430 cm^{-1} (~ 5%)	Adsorbed H_2O (stretching vibrations H-O-H)

In a research related to Raman spectroscopic images of bones [42] it has been demonstrated that strontium can heterogeneously distribute in bone mineral, with a higher amount in newly formed bone tissue than in old bone tissue. Additionally, it is shown that the strontium incorporation does not make any significant change in the crystal lattice parameters. In this study, in accordance with the infrared spectroscopy spectra, the Raman spectra of fluorapatite and strontium-magnesium-doped fluorapatites exhibit internal vibrational modes for the group of PO_4^{3-} , see Fig. 8. Thus, the most intense line of the

symmetric stretching vibration $\nu_1(\text{PO})$ at 961 cm^{-1} , which is a characteristic value for apatites [43], is clearly visible. According to [44], in the case of substitution of phosphate ions by carbonate ions, the phosphate line ν_1 appears in the range of $955\text{--}959\text{ cm}^{-1}$. The line of symmetric stretching vibration $\nu_1(\text{PO})$ was detected at 961 cm^{-1} . This fact indicates the high crystallinity of fluorapatite, which is confirmed by the XRD data (Fig. 4). In addition, the position of the ν_3 line (1038 cm^{-1}) corresponding to the asymmetric P-O stretching vibration did not change. For fluorapatite $\text{Ca}_8\text{SrMg}(\text{PO}_4)_6\text{F}_2$, a decrease in the intensity of the ν_3 line and its fusion with the extended ν_1 line are observed (Fig. 8b). In contrast to the ν_1 and ν_3 lines, the remaining lines of the P-O deformation vibrations ν_2 ($423\text{--}413\text{ cm}^{-1}$) and ν_4 ($596\text{--}606\text{ cm}^{-1}$) are shifted towards lower frequencies when calcium is replaced by strontium and magnesium. In addition, on the Raman spectra of fluorapatite and strontium-magnesium-containing fluorapatite, a 1077 cm^{-1} line was observed. This line is corresponded to CO_3^{2-} vibrations and indicated partial replacement of phosphate ions by carbonate ions ($\text{CO}_3^{2-} \rightarrow \text{PO}_4^{3-}$). The presence of CO_3^{2-} ions is caused by the absorption of atmospheric carbon dioxide by synthesized fluorapatite powders. It is known that the PO_4^{3-} tetrahedron in the fluorapatite lattice is surrounded by 9 calcium cations, which isolate it from other PO_4^{3-} tetrahedra. In [45] it is reported that the substitution of PO_4^{3-} ions by CO_3^{2-} ions does not cause any significant structural changes in the FAp structure that could be observed on the Raman spectra. These results are also in a good agreement with the IR analysis data.

Long-term immersion tests demonstrate the real behavior of the biomaterials in biological environment. In this regard, the solubility of the synthesized fluorapatites in physiological media and the effect of the structural replacement of calcium by strontium and magnesium are of great interest.

The results of the solubility tests of fluorapatites $\text{Ca}_{10}(\text{PO}_4)_6\text{F}_2$, and $\text{Ca}_8\text{MgSr}(\text{PO}_4)_6\text{F}_2$ in saline solution are shown in Fig. 9a. A decrease in the degree of dissolubility of fluorapatite in time was observed. These results also indicate a greater degree of solubility of strontium-magnesium substituted fluorapatite in comparison to unsubstituted fluorapatite. Fig. 9b shows the results of the solubility of the synthesized fluorapatites in buffer solution. It should be mentioned that in the previous study [38] an increase of the weight losses and dissolution rates of strontium substituted fluorapatite $\text{Ca}_9\text{Sr}(\text{PO}_4)_6\text{F}_2$ in comparison to unsubstituted fluorapatite $\text{Ca}_{10}(\text{PO}_4)_6\text{F}_2$ samples was detected. Based on [2], this fact is associated with the presence of tricalcium phosphate $\text{Ca}_3(\text{PO}_4)_2$ phase in the $\text{Ca}_9\text{Sr}(\text{PO}_4)_6\text{F}_2$ samples. It is known that tricalcium phosphate demonstrate greater solubility in comparison with fluorapatite. In the contrast, it was reported in [46] that the strontium and calcium substitutions cause no principal change in the dissolution rate of phosphate glasses. Additionally, the effect of strontium bonding to a similar number of phosphate chains as calcium was found. The addition of Sr into the phosphate glass composition resulted in a decrease of the dissolution rate of the glass, thus suggesting an increase of the cross-linking between phosphate chains. At present study, the results demonstrate that in both saline and buffer solutions the solubility of strontium-magnesium substituted fluorapatite is higher than fluorapatite. It

should be noted that in the buffer solution, the solubility of fluorapatites was not much higher than the solubility in saline.

There is a strong correlation between the structure, mechanical properties and solubility of ceramics. The ceramics with higher density and crystallinity demonstrate better mechanical characteristics and biocompatibility [47]. The hardness (H) to the Young's modulus (E) ratio is the main parameter, which characterizes the material deformation in relation to yielding [48]. H/E ratio plays an important role in identifying the mechanical behaviors and further brittle failure of ceramic materials and coatings [49]. Furthermore, fracture toughness (K_{1c}) parameters demonstrate the ability of a material to resist against brittle failure and crack propagation. Nanoindentation method allows to make direct measuring of cracks created with a sharp diamond indenter [50, 51].

Taking the above-mentioned points into consideration, the main mechanical parameters of $\text{Ca}_8\text{SrMg}(\text{PO}_4)_6\text{F}_2$ and $\text{Ca}_{10}(\text{PO}_4)_6\text{F}_2$ fluorapatites before and after immersion tests are presented in Table 2. The measured average value of Young's modulus on the surface of fluorapatite slightly exceeds the value for strontium-magnesium doped fluorapatite. After a solubility test in saline solution, the values of Young's modulus measured on the surface of both samples slightly decrease. On the contrary, microhardness and K_{1c} parameters for $\text{Ca}_8\text{SrMg}(\text{PO}_4)_6\text{F}_2$ samples decreased to a greater extent after immersion tests possibly due to the higher soluble tricalcium phosphate $\text{Ca}_3(\text{PO}_4)_2$ phase content.

Table 2. Young's modulus, hardness and fracture toughness parameters of fluorapatite samples before and after dissolution tests

Fluorapatites	Modulus, GPa		Hardness, GPa		K_{1c} , $\text{MPa} \cdot \text{m}^{1/2}$	
	Before dissolving	After dissolving	Before dissolving	After dissolving	Before dissolving	After dissolving
$\text{Ca}_{10}(\text{PO}_4)_6\text{F}_2$	106.3±4.5	97.7±6.1	5.9±1.1	5.2±0.6	2.0±0.9	1.7±0.5
$\text{Ca}_8\text{MgSr}(\text{PO}_4)_6\text{F}_2$	102.7±5.3	93.4±4.7	5.5±0.7	4.1±1.9	1.8±0.4	1.3±0.8

Nevertheless, the dissolution of the synthesized fluorapatites within 14 days occurs to a small extent and does not significantly affect their mechanical properties.

The surface of fluorapatite samples after 14 days of immersion tests in saline solution was studied by Raman spectroscopy, SEM, and laser confocal microscopy.

An analysis of the Raman spectra of the surface of fluorapatite samples after solubility tests also showed the presence of the main fluorapatite lines $\nu_1(\text{P-O})$ at 965 cm^{-1} , see Fig. 10. These results indicate a strong stability of fluorapatite and strontium-magnesium-doped fluorapatite in saline solution at a temperature of $37 \text{ }^\circ\text{C}$. The presence of the ν_1 peak in the Raman spectrum confirms the stability of the crystal structure of fluorapatite on the surface of the studied samples. After solubility tests for

$\text{Ca}_{10}(\text{PO}_4)_6\text{F}_2$ fluorapatite, a shift to the region of high frequencies of the line ν_3 ($1038 \rightarrow 1052 \text{ cm}^{-1}$) and low frequencies of the line ν_2 ($423 \rightarrow 430 \text{ cm}^{-1}$) were observed in (Fig. 10a). On the contrary, the line ν_4 was shifted to the low frequencies region ($596 \rightarrow 588 \text{ cm}^{-1}$). At the same time, the position of the line corresponded to the vibrations of CO_3^{2-} ($1077 \rightarrow 1079 \text{ cm}^{-1}$) was almost unchanged. For $\text{Ca}_8\text{MgSr}(\text{PO}_4)_6\text{F}_2$ fluorapatite after immersion tests, shift of the lines of P-O deformation vibration ν_2 ($413 \rightarrow 425 \text{ cm}^{-1}$) and ν_4 ($606 \rightarrow 628 \text{ cm}^{-1}$) towards higher frequencies was detected (Fig. 10b).

The position of the line corresponding to the vibrations of CO_3^{2-} was also significantly changed ($1077 \rightarrow 1088 \text{ cm}^{-1}$). It is known that the solubility of apatite increases as a result of the replacing the PO_4^{3-} ions with the CO_3^{2-} ions. The higher solubility of carbonate-containing apatite compared to carbonate-free apatite is partially due to the fact that $\text{Ca}^{2+}\text{-CO}_3^{2-}$ bonds are weaker than $\text{Ca}^{2+}\text{-PO}_4^{3-}$ bonds [52].

The presence of a second, more soluble, $\text{Ca}_3(\text{PO}_4)_2$ phase and partial replacement of phosphorus ions by carbon ions led to increasing in solubility level and, accordingly, to changes in the surface of fluorapatite samples after dissolution, which are reflected in the Raman spectra.

The surfaces of the $\text{Ca}_{10}(\text{PO}_4)_6\text{F}_2$ and $\text{Ca}_8\text{MgSr}(\text{PO}_4)_6\text{F}_2$ samples after immersion tests, are significantly different, see Fig. 11a and Fig. 11b. It is noticeable that the surface of the $\text{Ca}_8\text{MgSr}(\text{PO}_4)_6\text{F}_2$ sample underwent stronger dissolution as compared to $\text{Ca}_{10}(\text{PO}_4)_6\text{F}_2$, see Fig. 11c and Fig. 11d.

According to the data of EDX analysis of surface after soaking tests, the main peaks of Ca, P, O, F, Sr and Mg corresponding to the elemental composition of fluorapatites are identified in Fig.12.

The EDX spectra demonstrate some changes in the peak intensity after immersion tests. A noticeable decrease of the fluorine content in the composition of the fluorapatites samples was detected. C. Chairat et al [53] argue that the dissolution of apatite is primarily due to the relatively rapid removal of F and Ca from the contact surface. Thus, the destruction of fluorapatite occurs due to the breaking of Ca-O bonds on the surface depleted of calcium and fluorine.

The stability of structure, phase composition, and mechanical properties during long term period of staying in biological environment is very important for biocompatibility of ceramics, if they are used as a biomaterial. Thus, both the $\text{Ca}_{10}(\text{PO}_4)_6\text{F}_2$ and $\text{Ca}_8\text{MgSr}(\text{PO}_4)_6\text{F}_2$ fluorapatites can be further proposed as promising candidates for biomedical use in the replacement of defective areas of bone.

4. Conclusion

At present study the powders of monophasic fluorapatite $\text{Ca}_{10}(\text{PO}_4)_6\text{F}_2$ and strontium-magnesium doped fluorapatite $\text{Ca}_8\text{MgSr}(\text{PO}_4)_6\text{F}_2$ were obtained by chemical precipitation method. Then the dense samples

of fluorapatites: $\text{Ca}_{10}(\text{PO}_4)_6\text{F}_2$ and $\text{Ca}_8\text{MgSr}(\text{PO}_4)_6\text{F}_2$ were produced after sintering at the temperature of 1250 °C for 6 hours in air. The XRD and Raman spectrometry data demonstrate a high crystallinity of the fluorapatite and strontium-magnesium-doped fluorapatites. The phase composition of obtained fluorapatites was represented by the main phases of $\text{Ca}_{10}(\text{PO}_4)_6\text{F}_2$ and $\text{Ca}_8\text{MgSr}(\text{PO}_4)_6\text{F}_2$, respectively. A concomitant phase of the tricalcium phosphate $\text{Ca}_3(\text{PO}_4)_2$ was also presented mainly in the composition of strontium-magnesium doped fluorapatite. The immersion tests in saline and buffer solutions indicated a greater degree of solubility of strontium-magnesium substituted fluorapatite in comparison to unsubstituted fluorapatite. According to scanning electron and laser confocal microscopy analysis, a pronounced surface dissolution of the strontium-magnesium doped fluorapatite sample was observed. The mechanical parameters of fluorapatites such as Young's modulus, hardness, and fracture toughness measured on the surface of the samples slightly decrease for both fluorapatite and strontium-magnesium doped fluorapatite after immersion tests.

Results demonstrate stability of structural properties of fluorapatites after soaking in saline and buffer solutions. The durability of mechanical properties and biocompatibility of $\text{Ca}_{10}(\text{PO}_4)_6\text{F}_2$ and $\text{Ca}_8\text{MgSr}(\text{PO}_4)_6\text{F}_2$ fluorapatites make these materials highly attractive for biomedical applications.

Declarations

Author Contributions

The manuscript was written through contributions of all authors. All authors have given approval to the final version of the manuscript.

Notes

The authors declare no competing financial interest.

References

1. Terra, F. Audubert, N. Dacheux, C. Guy, R. Podor, Synthesis and characterization of thorium-bearing britholites, *Journal of Nuclear Materials*, 354 (2006) 49–65.
2. A. Shkuropatenko, S. Y. Sayenko, K. A. Ulybkina, A. V. Zykova, L. M. Lytvynenko, A. G. Myronova, Phase composition, structure, corrosion and radiation resistance of synthesized $\text{Ca}_{10}(\text{PO}_4)_6\text{F}_2$ and $\text{Ca}_9\text{Sr}(\text{PO}_4)_6\text{F}_2$ fluorapatites, *Functional materials*, 26 (1) (2019) 71-77.
3. Ramesha, K. L. Aw, R. Tolouei, M. Amiriyani, C. Y. Tan, M. Hamdi, J. Purbolaksono, M. A. Hassan, W. D. Teng, Sintering properties of hydroxyapatite powders prepared using different methods, *Ceramics International*, 39 (2013) 111–119.
4. Landi, A. Tampieri, G. Celotti, S. Sprio, M. Sandri, G. Logroscino, Sr-substituted hydroxyapatites for osteoporotic bone replacement, *Acta Biomaterialia*, 3 (2007) 961–969

5. Tacail, L. Kovačiková, J. Brůžek, V. Balter, Spatial distribution of trace element Ca-normalized ratios in primary and permanent human tooth enamel, *Sci. Total Environment*, 603–604 (2017) 308–318
6. Christoffersen, M. R. Christoffersen, N. Kolthoff, O. Barenholdt, Effects of strontium ions on growth and dissolution of hydroxyapatite and on bone mineral detection, *Bone*, 20 (1997) 47–54.
7. Montazeri, J. Javadpour, M. A. Shokrgozar, S. Bonakdar, S. Javadian, Hydrothermal synthesis and characterization of hydroxyapatite and fluorhydroxyapatite nanosize powders, *Biomedical Materials*, 5 (2010) 1–7.
8. Hanifi, M. H. Fathi, H. M. Sadeghi, J. Varshosaz, Mg²⁺ substituted calcium phosphate nano particles synthesis for non viral gene delivery application, *Journal of Material Science: Materials in Medicine*, 21 (2010) 2393–2401.
9. Zhang, Y. S. Wang, X. T. Zeng, K. A. Khor, W. Weng, D. E. Sun, Evaluation of adhesion strength and toughness of fluoridated hydroxyapatite coatings, *Thin Solid Films*, 516 (2008) 5162–5167.
10. Cai, S. Zhang, X. Zeng, M. Qian, D. Sun, W. Weng, Interfacial study of magnesium-containing fluoridated hydroxyapatite coatings, *Thin Solid Films*, 519 (2011) 4629–4633.
11. Kheradmandfard, M. H. Fathi, M. Ahangarian, E. M Zahrani, In vitro bioactivity evaluation of magnesium-substituted fluorapatite nanopowders, *Ceramics International*, 38 (2012) 169–175.
12. Kheradmandfard, M. H. Fathi, Fabrication and characterization of nanocrystalline Mg-substituted fluorapatite by high energy ball milling, *Ceramics International*, 39 (2013) 1651–1658.
13. Cai, S. Zhang, X. Zeng, Y. Wang, M. Qian, W. Weng, Improvement of bioactivity with magnesium and fluorine ions incorporated hydroxyapatite coatings via sol–gel deposition on Ti6Al4V alloys, *Thin Solid Films*, 517 (2009) 5347–5351.
14. Sharifnabi, M. H. Fathi, B. Eftekhari Yektaa, M. Hossainlipour, The structural and bio-corrosion barrier performance of Mg-substituted fluorapatite coating on 316L stainless steel human body implant, *Applied Surface Science*, 288 (2014) 331– 340
15. W. Kim, Y. M. Kong, C. J. Bae, Y. J. Noh, H. E. Kim, Sol–gel derived fluor-hydroxyapatite biocoatings on zirconia substrate, *Biomaterials*, 25 (2004) 2919–2926.
16. Basar, A. Tezcaner, D. Keskin, Z. Evis, Improvements in microstructural, mechanical, and biocompatibility properties of nanosized hydroxyapatites doped with yttrium and fluoride, *Ceramics International*, 36 (2010) 1633–1643.
17. Cacciotti, Bivalent cationic ions doped bioactive glasses: the influence of magnesium, zinc, strontium and copper on the physical and biological properties, *Journal of Materials Science*, 52 (2017) 8812–8831.
18. Dietrich, H. Oudadesse, A. Lucas-Girot, Y.L. Gal, S. Jeanne, G. Cathelineau, Effect of Mg and Zn on the surface of doped melt-derived glass for biomedical applications, *Applied Surface Science*, 255 (2008) 391-395.
19. H. Qi, S. Zhang, K.A. Khor, W. Weng, X. Zeng, C. Liu, In vitro effect of magnesium inclusion in sol-gel derived apatite, *Thin Solid Films*, 516 (2008) 5172-5175.

20. D. Grynblas, E. Hamilton, R. Cheung, Y. Tsouderos, P. Deloffre, M. Hott, P. J. Marie, Strontium increases vertebral bone volume in rats at a low dose that does not induce detectable mineralization defect, *Bone*, 18 (1996) 253–259.
21. Saidak, P. J. Marie, Strontium signaling: Molecular mechanisms and therapeutic implications in osteoporosis, *Pharmacology&Therapeutics*, 136 (2012) 216–226.
22. J. Marie, Strontium as therapy for osteoporosis, *Current Opinion in Pharmacology*, 5 (2005) 633–636.
23. Gentleman, Y. C. Fredholm, G. Jell, N. Lotfibakhshaiesh, M. D. O'Donnell, R. G. Hill, et al., The effects of strontium-substituted bioactive glasses on osteoblasts and osteoclasts in vitro, *Biomaterials*, 31 (2010) 3949–3956.
24. Kargozar, N. Lotfibakhshaiesh, J. Ai, A. Samadikuchaksaraie, R. G. Hill, P. A. Shah, et al., Synthesis, physico-chemical and biological characterization of strontium and cobalt substituted bioactive glasses for bone tissue engineering, *Journal of Non-Crystalline Solids*, 449 (2016) 133–140.
25. Pina, P. Torres, F. Goetz-Neunhoeffler, J. Neubauer, J. Ferreira, Newly developed Sr-substituted α -TCP bone cements, *Acta Biomaterialia*, 6 (2010) 928–935.
26. Kuda, N. Pinchuk, O. Bykov, T. Tomila, O. Olifan, M. Golovkova, Development and characterization of Sr-containing glass-ceramic composites based on biogenic hydroxyapatite, *Nanoscale Research Letters*, 13 (2018) 155.
27. Saboori, M. Rabiee, F. Moztarzadeh, M. Sheikhi, M. Tahriri, M. Karimi, Synthesis, characterization and in vitro bioactivity of sol-gel-derived SiO_2 –CaO– P_2O_5 –MgO bioglass, *Materials Science and Engineering C*, 29 (2009) 335–340.
28. Mróz, A. Bombalska, S. Burdyn'ka, M. Jedyn'ki, A. Prokopiuk, B. Budner, A. Slósarczyk, A. Zima, E. Menaszek, A. Scisłowska-Czarnecka, K. Niedzielski, Structural studies of magnesium doped hydroxyapatite coatings after osteoblast culture, *Journal of Molecular Structure*, 977 (2010) 145–152.
29. Ren, Y. Leng, R. Xin, X. Ge, Synthesis, characterization and ab initio simulation of magnesium-substituted hydroxyapatite, *Acta Biomaterialia*, 6 (2010) 2787–2796.
30. M. Ko, K. Lee, B. H. Kim, Effect of Mg ion on formation of bone-like apatite on the plasma modified titanium surface, *Surface&Coatings Technology*, 228 (2013) S404I–S407.
31. Weiss, R. Torres, S. Buchner, S. Blunk, P. Soares, Effect of Ti and Mg dopants on the mechanical properties, solubility, and bioactivity in vitro of a Sr-containing phosphate based glass. *Journal of Non-Crystalline Solids*, 386 (2014) 34–38.
32. Kapoor, A. Goel, A. Tilocca, V. Dhuna, G. Bhatia, K. Dhuna, et al., Role of glass structure in defining the chemical dissolution behavior, bioactivity and antioxidant properties of zinc and strontium co-doped alkali-free phosphosilicate glasses. *Acta Biomaterialia*, 10 (2014) 3264–3278.
33. Kapoor, A. Goel, M. J. Pascual. J. M Ferreira, Thermo-mechanical behaviour of alkali free bioactive glass-ceramics co-doped with strontium and zinc. *Journal of Non-Crystalline Solids*, 375 (2013) 74–82.

34. Stefanic, M. Peroglio, A.M. Stanciuc, G. Machado, L. Campbell, M. M. Krzmanc, M. Alini, X. Zhang, The influence of strontium release rate from bioactive phosphate glasses on osteogenic differentiation of human mesenchymal stem cells, *Journal of the European Ceramic Society*, 38 (2018) 887–897.
35. Liu, S. C. Rawlinson, R. G. Hill, F. Fortune, Strontium-substituted bioactive glasses in vitro osteogenic and antibacterial effects, *Dental Materials*, 32 (2016) 412–422.
36. S. Brauer, N. Karpukhina, G. Kedia, A. Bhat, R. V. Law, I. Radecka, R. G. Hill, Bactericidal strontium-releasing injectable bone cements based on bioactive glass, *Journal of the Royal Society Interface*, 10(78) (2013) 20120647.
37. Zhang, S. Zhao, Y. Zhu, Y. Huang, M. Zhu, C. Tao, et al., Three-dimensional printing of strontium-containing mesoporous bioactive glass scaffolds for bone regeneration, *Acta Biomaterialia*, 10 (2014) 2269–2281.
38. Yu. Sayenko, Obtaining of strontium doped fluorapatite powders, *Functional Materials*, 22(2) (2015) 263-268.
39. Kheradmandfard, M. H. Fathi, F. Ansari, T. Ahmadi, Effect of Mg content on the bioactivity and biocompatibility of Mg-substituted fluorapatite nanopowders fabricated via mechanical activation, *Materials Science and Engineering C*, 68 (2016) 136–142.
40. V. Chaikina, Mechanic chemical processes and the mechanism of energy conversion during indentation of single crystals, *Chemistry for Sustainable Development*, 17 (2009) 653–666.
41. C. Farmer. *The infrared spectra of minerals*, Mineralogical society, London, 1974, 539 p.
42. G. Dahl, P. Allain, P. J. Marie, Y. Mauras, G. Boivin, P. Ammann, Y. Tsouderos, P. D. Delmas, C. Christiansen, Incorporation and Distribution of Strontium in Bone. *Bone*, 28(4) (2001) 446-453.
43. Huaguang, H. Zhang, X. Wang, Z. Gu, X. Li, F. Deng, Local structure of hydroxyl-peroxy apatite: A combined XRD, FT-IR, Raman, SEM, and solid-state NMR study, *Journal of Physics and Chemistry of Solids*, 68 (2007) 1863–1871.
44. P. Tarnowski, M. A. Ignelzi Jr, M. D. Morris, Mineralization of Developing Mouse Calvaria as Revealed by Raman Microspectroscopy, *Journal of Bone and Mineral Research*, 17(6) (2002) 1118–1126.
45. Leroy, G. Penel, N. Leroy, E. Bres, Human Tooth Enamel: A Raman Polarized Approach, *Applied Spectroscopy*, 56 (2002) 1030-1034.
46. Patel, R. Moss, K. M. Z. Hossain, A. R. Kennedy, E. R. Barney, A. C. Hannon, et al., Structural and physico-chemical analysis of calcium/strontium substituted, near-invert phosphate based glasses for biomedical applications, *Acta Biomaterialia*, 60 (2017) 109–127.
47. W. Kim, J. C. Knowles, L. Li, H. E. Kim, Mechanical performance and osteoblast-like cell responses of fluorine-substituted hydroxyapatite and zirconia dense composite, *Journal Biomedical Material Research B: Applied Biomaterials*, 70 (2004) 258-268.
48. L. Joslin, W. C. Oliver, A New Method for Analyzing Data from Continuous Depth-Sensing Microindentation Tests, *Journal of Materials Research*, 5(1) (1990) 123-126.

49. Leyland, A. Matthews, On the Significance of the H/E Ratio in Wear Control: a Nanocomposite Coating Approach to Optimised Tribological Behaviour, *Wear*, 246(1-2) (2000) 1-11.
50. T. Laugier, New formula for indentation toughness in ceramics, *Journal of Material Science Letters*, 6 (1987) 355-366.
51. R. Lawn, *Fracture of brittle solids*, Cambridge, UK: Cambridge University Press; 1993. Chapter 8
52. Wopenka, J. D. Pasteris, A mineralogical perspective on the apatite in bone, *Materials Science and Engineering C*, 25(2) (2005) 131-143.
53. Chairat, J. Schott, E. H. Oelkers, J. E. Lartigue, N. Harouiya, Kinetics and mechanism of natural fluorapatite dissolution at 25°C and pH from 3 to 12, *Geochimica et Cosmochimica Acta*, 71 (2007) 5901-5912.

Figures

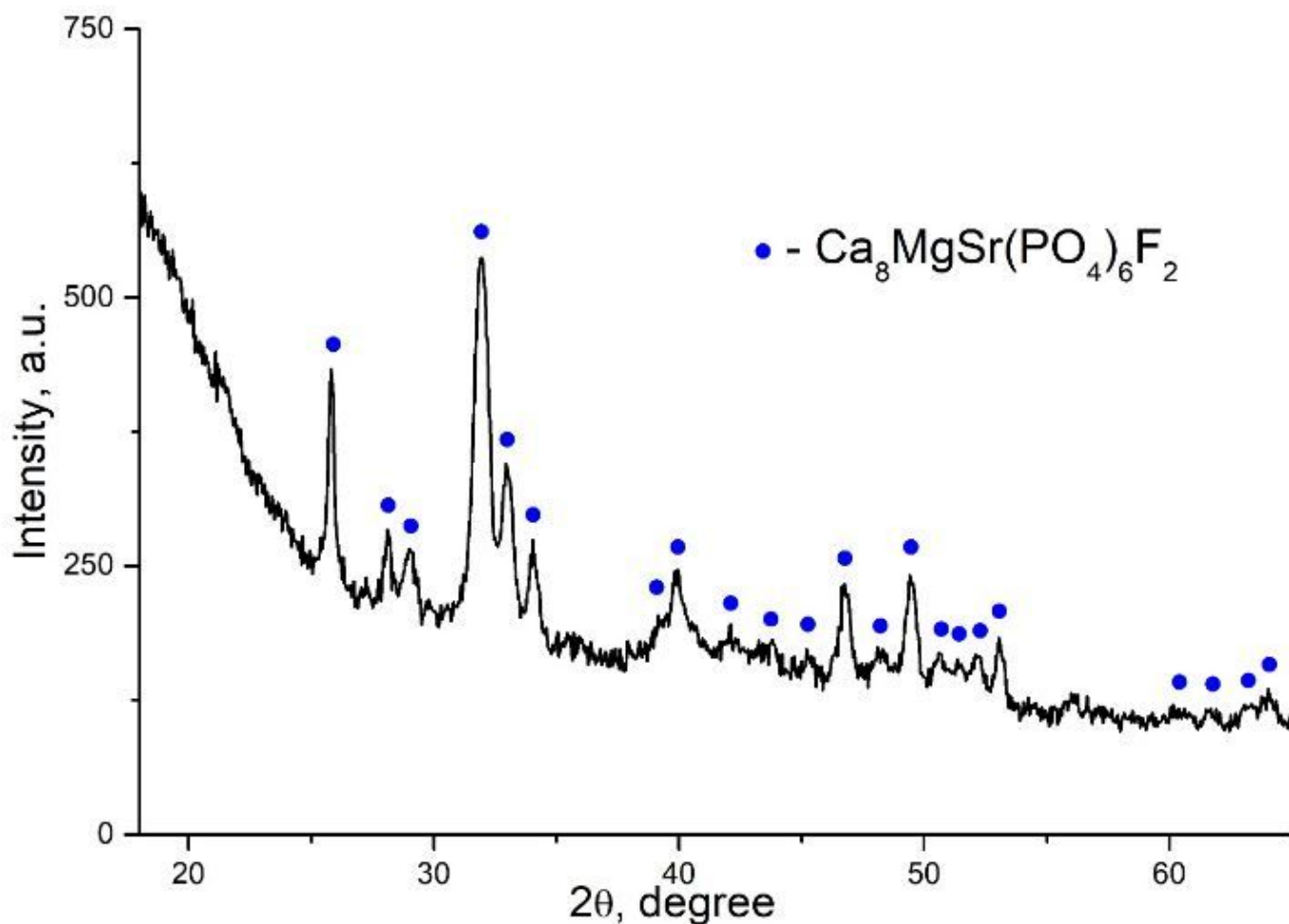
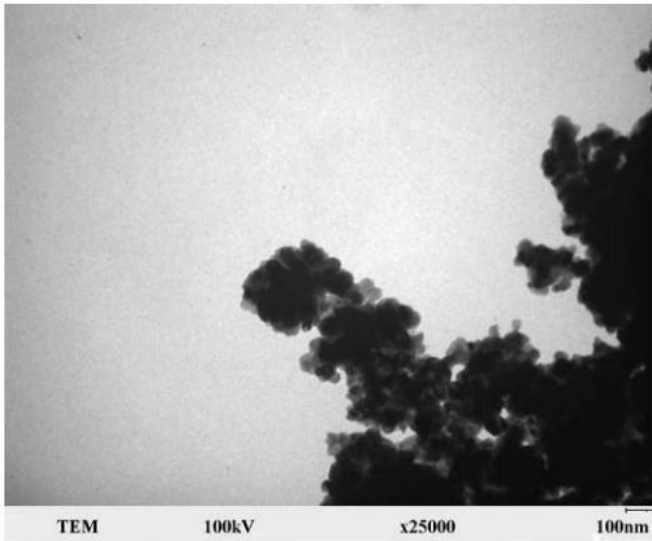
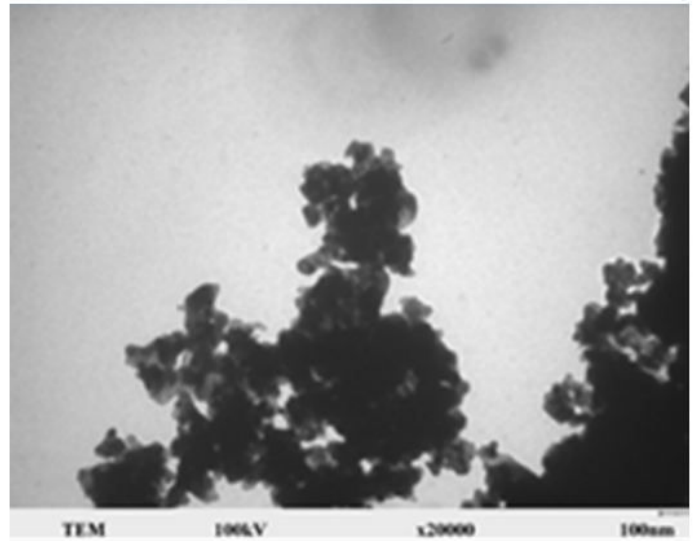


Figure 1

Diffractogram of powder of synthesized fluorapatite $\text{Ca}_8\text{MgSr}(\text{PO}_4)_6\text{F}_2$



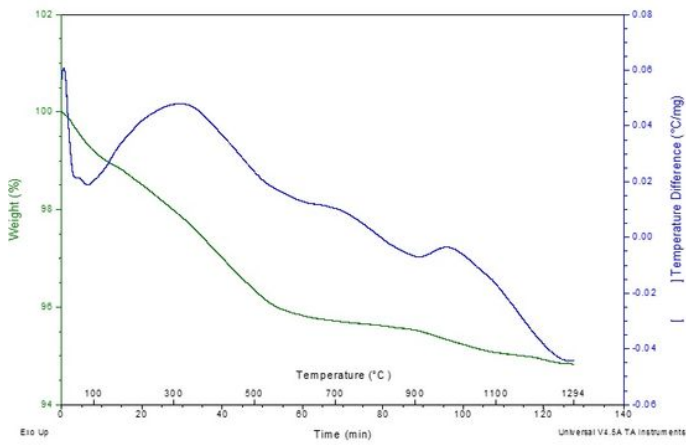
a



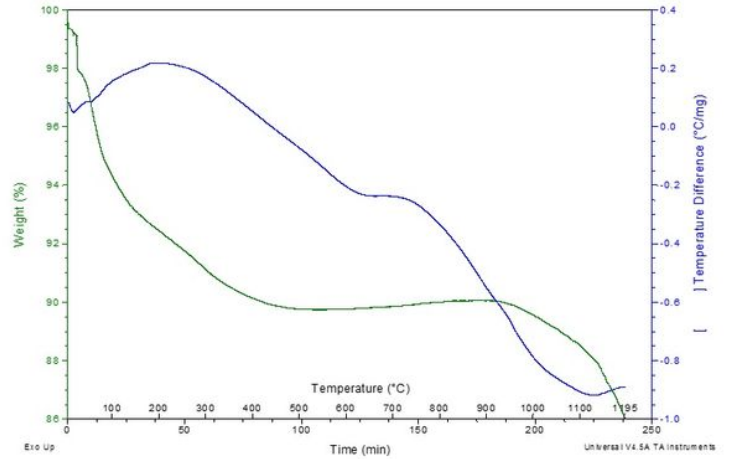
b

Figure 2

Transparent electron microscopy (TEM) of $\text{Ca}_{10}(\text{PO}_4)_6\text{F}_2$ (a) and $\text{Ca}_8\text{MgSr}(\text{PO}_4)_6\text{F}_2$ (b) powders obtained by chemical co-precipitation



a



b

Figure 3

DTA/TGA $\text{Ca}_{10}(\text{PO}_4)_6\text{F}_2$ (a) and $\text{Ca}_8\text{MgSr}(\text{PO}_4)_6\text{F}_2$ (b)

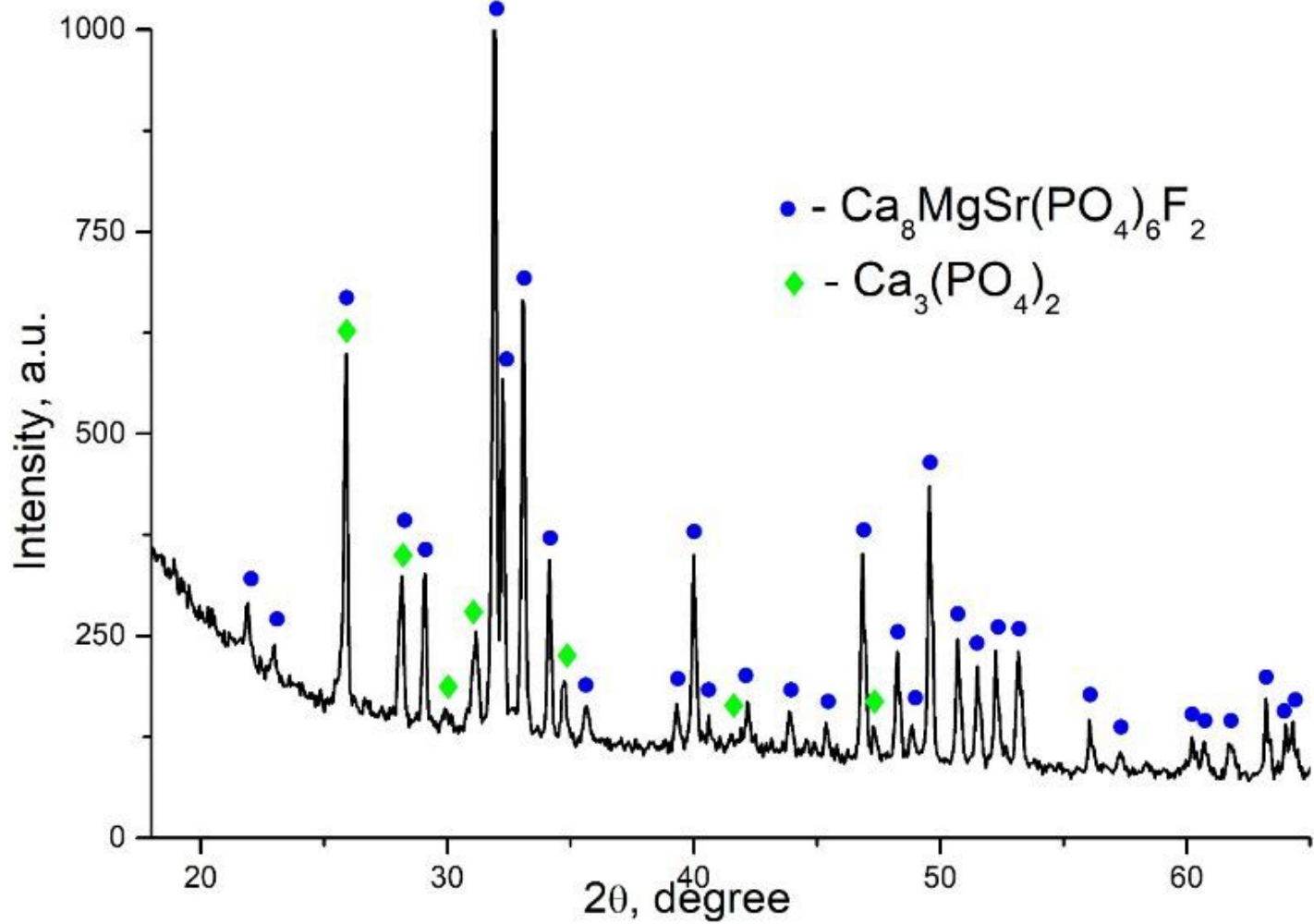
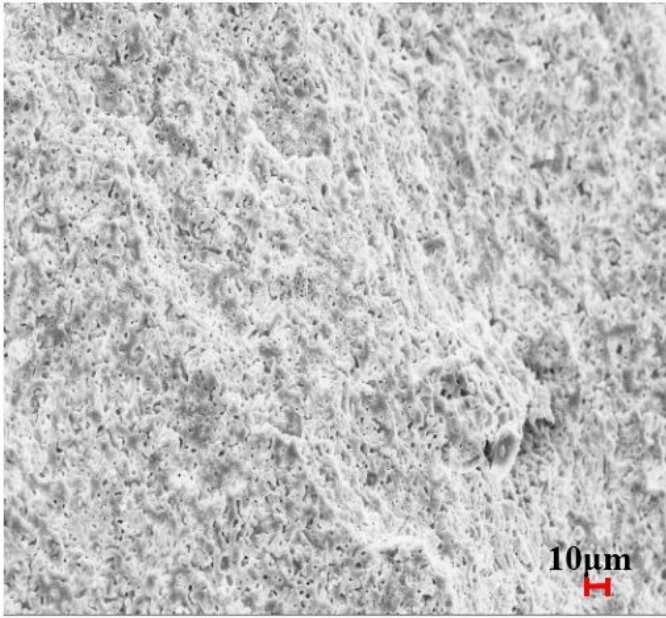
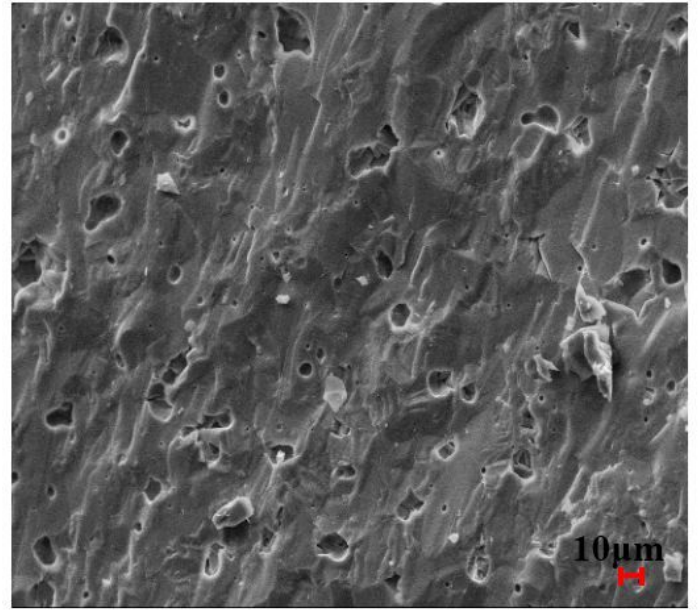


Figure 4

Diffraction pattern of sample $\text{Ca}_8\text{MgSr}(\text{PO}_4)_6\text{F}_2$ after sintering (1250 °C, 6 hours)



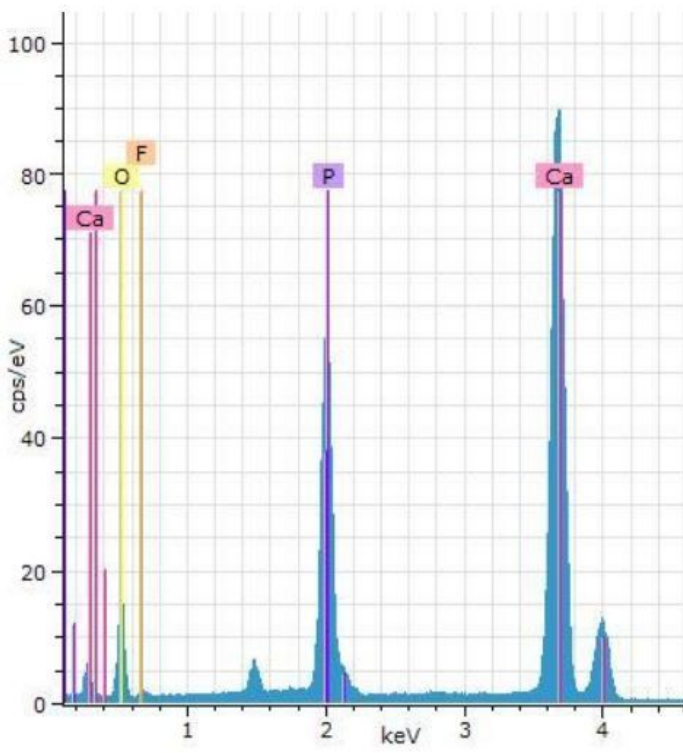
a



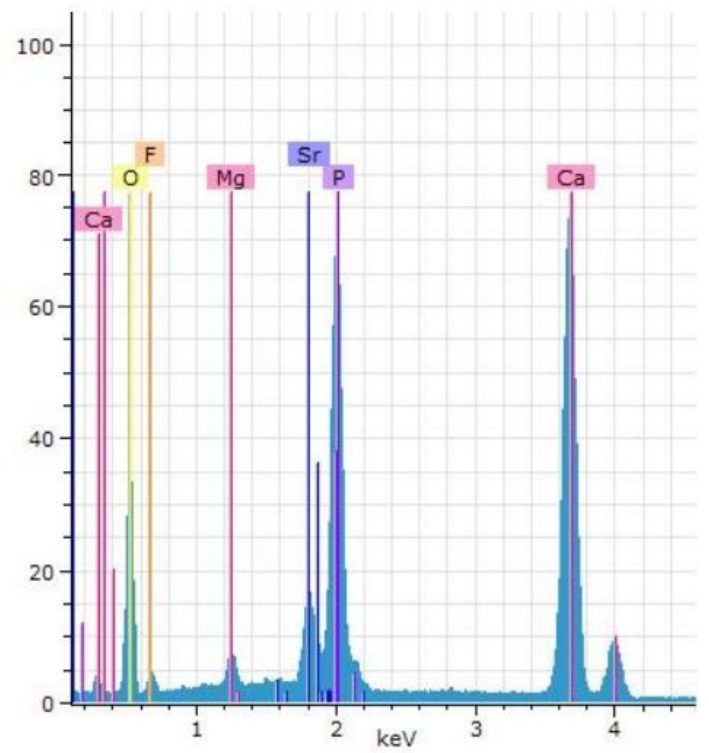
b

Figure 5

Cleaved surface structure of (a) $\text{Ca}_{10}(\text{PO}_4)_6\text{F}_2$ and (b) $\text{Ca}_8\text{MgSr}(\text{PO}_4)_6\text{F}_2$ samples



a



b

Figure 6

Elemental composition of fluorapatite samples of $\text{Ca}_{10}(\text{PO}_4)_6\text{F}_2$ (a) and $\text{Ca}_8\text{MgSr}(\text{PO}_4)_6\text{F}_2$ (b) samples

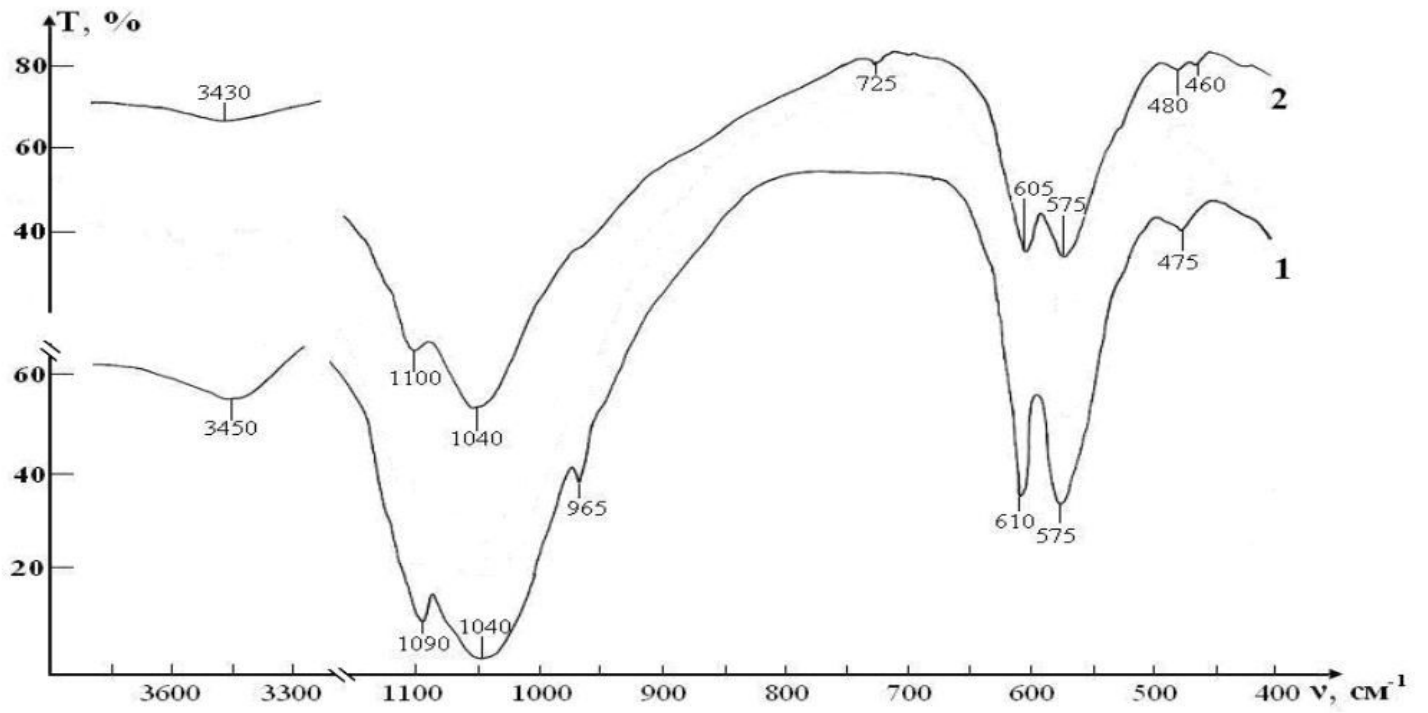
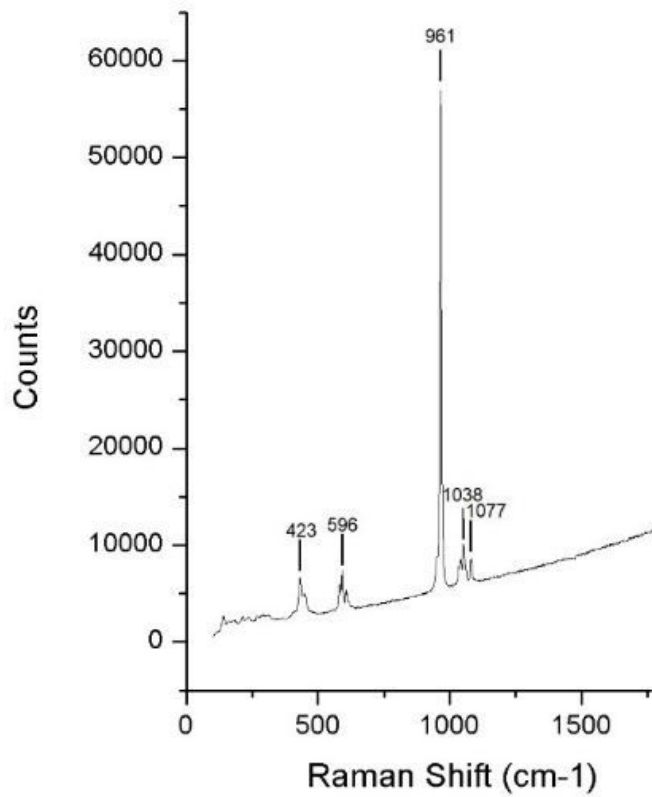
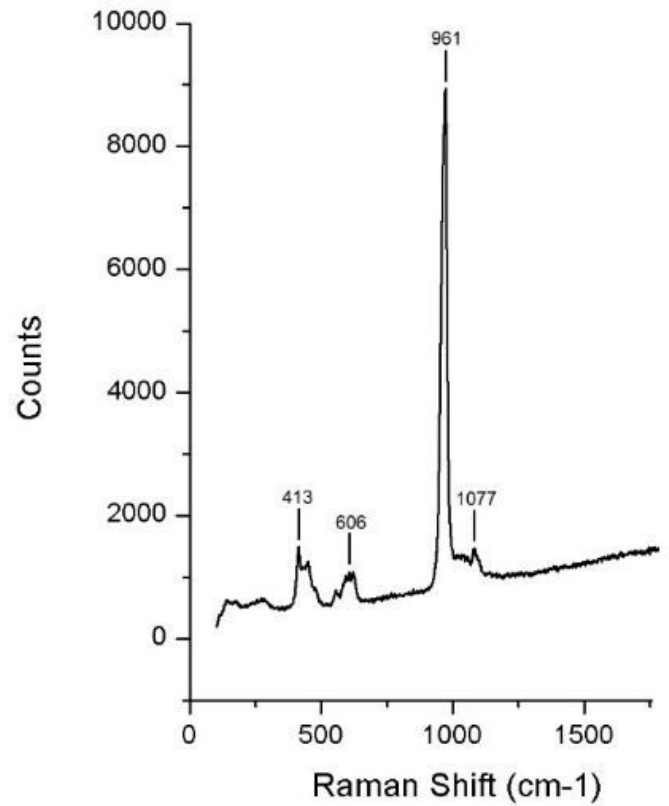


Figure 7

IR absorption spectra of fluorapatites: 1 - $\text{Ca}_{10}(\text{PO}_4)_6\text{F}_2$, 2 - $\text{Ca}_8\text{SrMg}(\text{PO}_4)_6\text{F}_2$



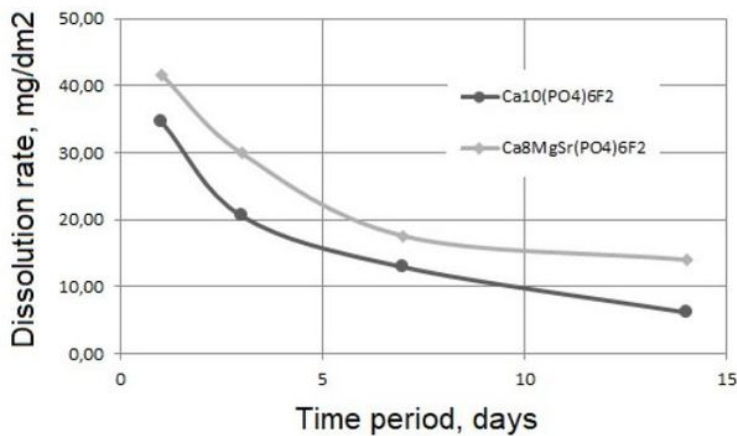
a



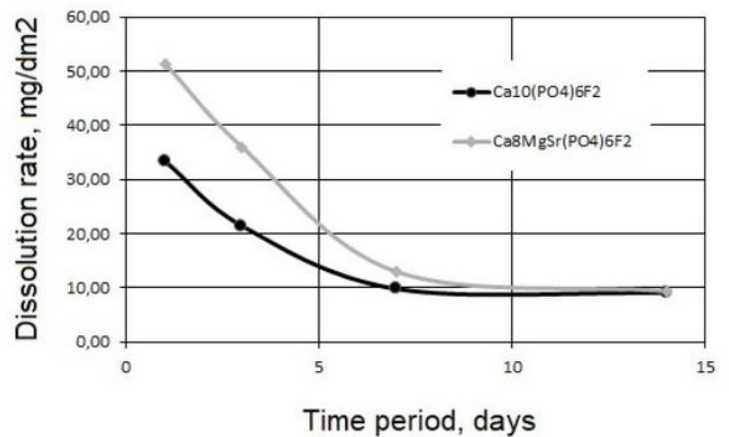
b

Figure 8

Raman spectra of fluorapatites $\text{Ca}_{10}(\text{PO}_4)_6\text{F}_2$ (a), and $\text{Ca}_8\text{MgSr}(\text{PO}_4)_6\text{F}_2$ (b)



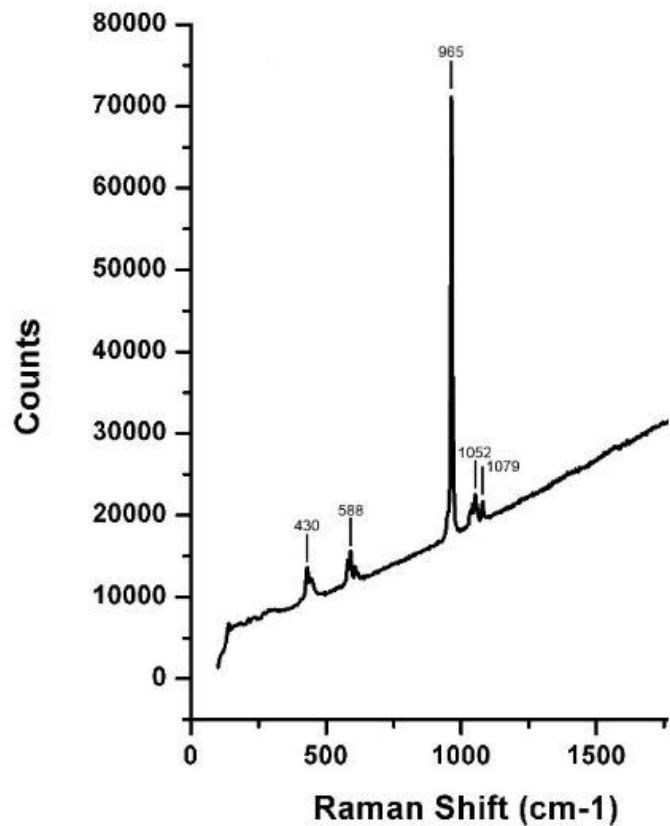
a



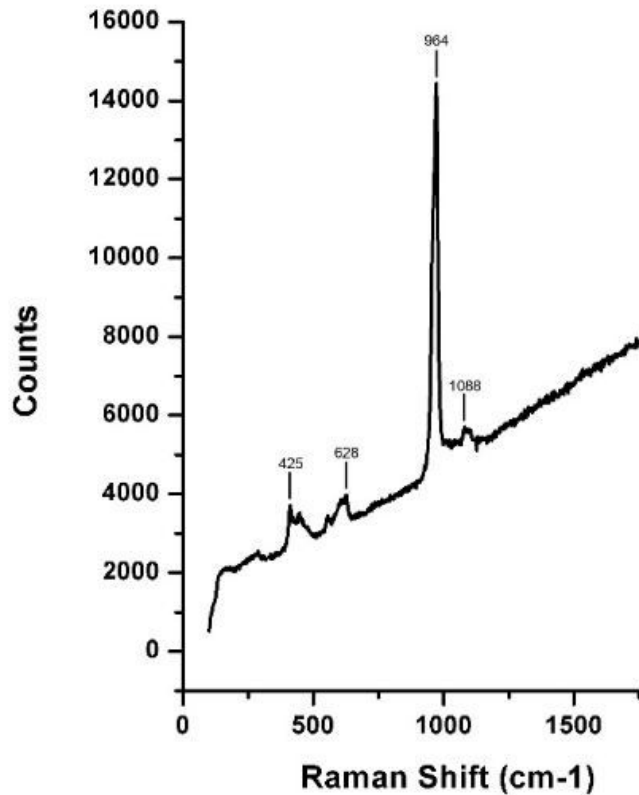
b

Figure 9

Dissolution rate of the obtained fluorapatite samples $\text{Ca}_{10}(\text{PO}_4)_6\text{F}_2$ and $\text{Ca}_8\text{SrMg}(\text{PO}_4)_6\text{F}_2$ in saline (a) and buffer solution (b)



a



b

Figure 10

Raman spectra of fluorapatites $\text{Ca}_{10}(\text{PO}_4)_6\text{F}_2$ (a) and $\text{Ca}_8\text{MgSr}(\text{PO}_4)_6\text{F}_2$ (b) after solubility tests.

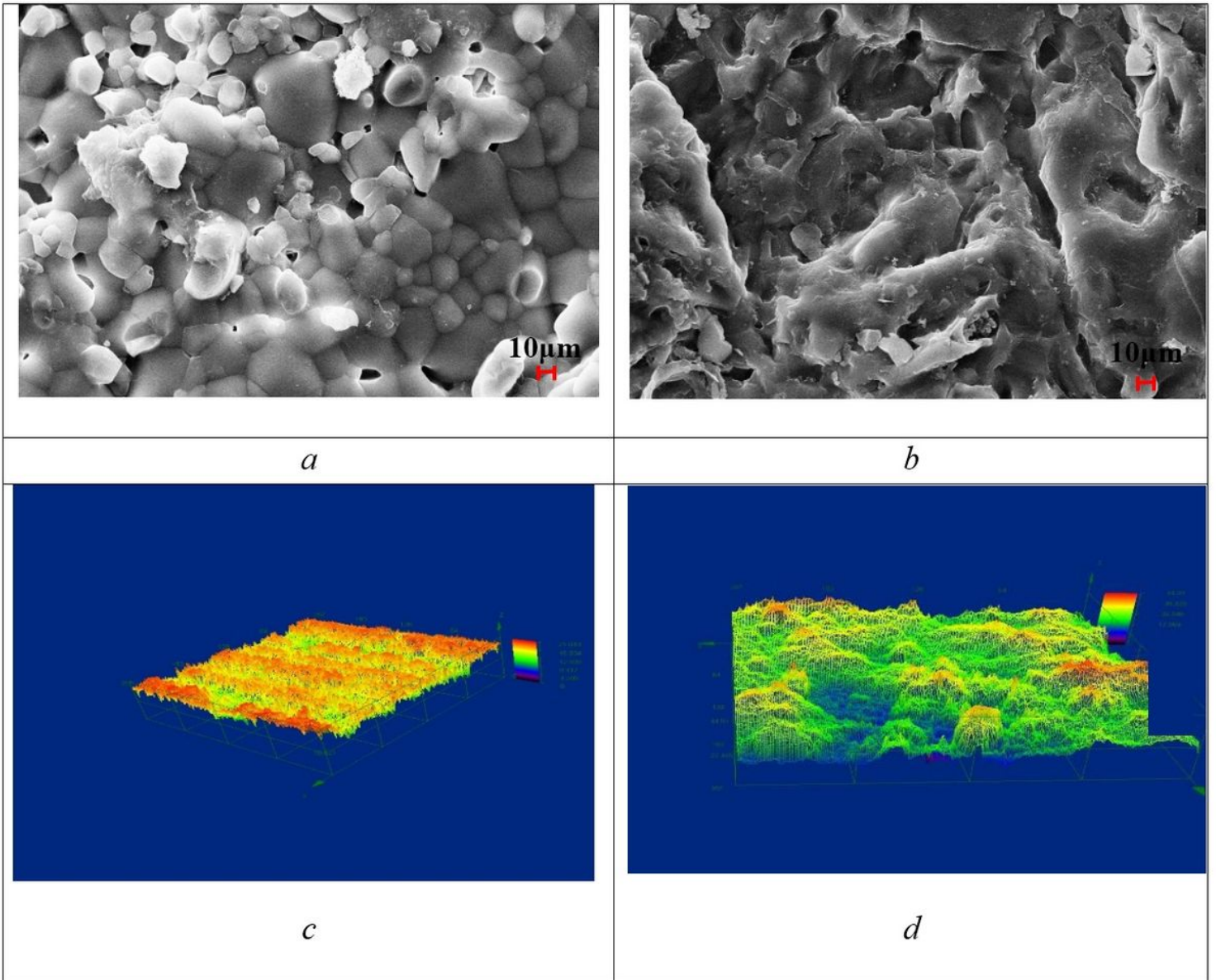
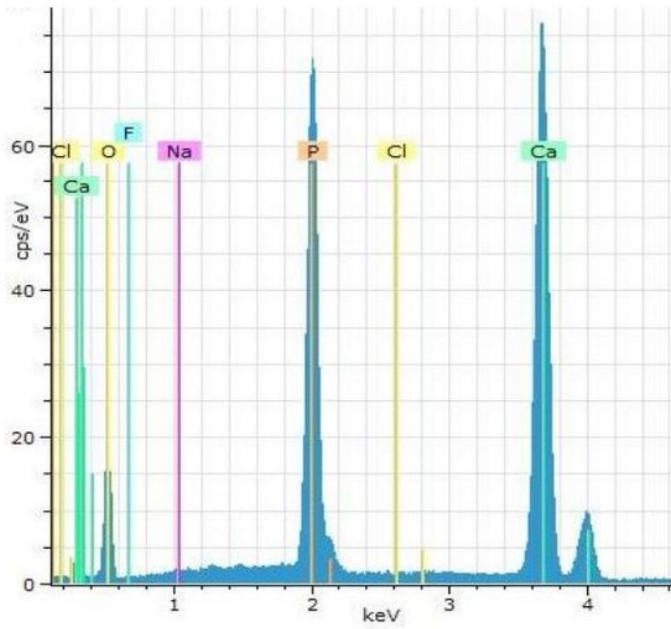
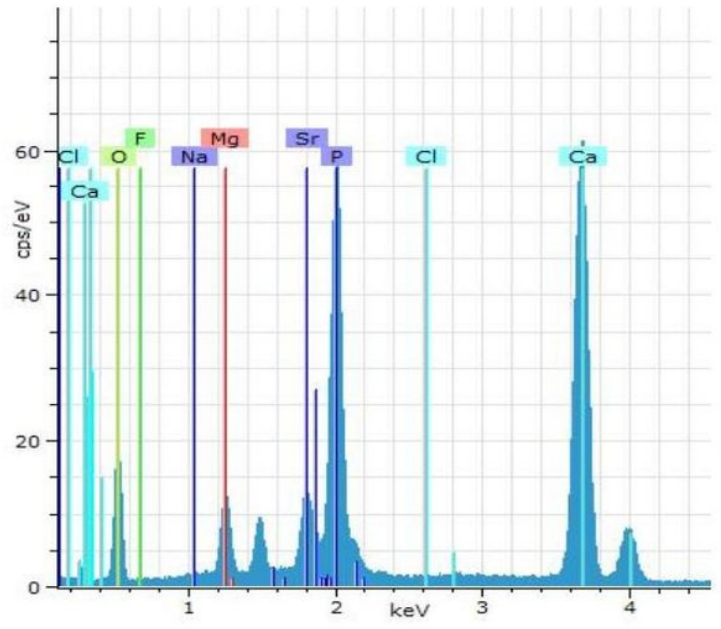


Figure 11

The surface structure and topography of the samples $\text{Ca}_{10}(\text{PO}_4)_6\text{F}_2$ (a, c) and $\text{Ca}_8\text{MgSr}(\text{PO}_4)_6\text{F}_2$ (b, d) after immersion tests



a



b

Figure 12

Elemental composition of fluoroapatite samples of (a) $\text{Ca}_{10}(\text{PO}_4)_6\text{F}_2$ and (b) $\text{Ca}_8\text{MgSr}(\text{PO}_4)_6\text{F}_2$ after dissolution tests